Check for updates

Ratiometric fluorescent nanosensors for ultra-sensitive detection of mercury ions based on AuNCs/MOFs†

Xi-Jin Wu, Fan Kong, Chun-Qin Zhao and Shou-Nian Ding ⓘD *

Ratiometric fluorescent nanosensors were developed to detect mercury ions (Hg^{2+}) using enhanced dual emissions from glutathione stabilized gold nanoclusters/indium-based metal–organic frameworks modified with cysteine (AuNCs/MIL-68(In)-NH$_2$/Cys). The nanosensors exhibited bright pink fluorescence with AuNCs evenly distributed on MIL-68(In)-NH$_2$. Under 370 nm excitation, the obtained sensor presented double fluorescence emission around 438 nm and 668 nm, which was attributed to MIL-68(In)-NH$_2$ and GSH-AuNCs, respectively. The fluorescence emission was remarkably enhanced after modification with Cys. In the presence of Hg^{2+}, the red fluorescence peak at 668 nm was quenched, while the blue fluorescence peak at 438 nm was slightly altered. The prepared AuNCs/MIL-68(In)-NH$_2$/Cys nanosensors exhibited two linear ranges for the detection of Hg^{2+}, namely from 20 pM to 0.2 μM and 0.2 μM to 60 μM, with a detection limit of 6.7 pM. They also presented high selectivity towards other ions and good performance in real water samples. Moreover, a radial star-shaped microfluidic paper-based analytical device (μPAD), as a straightforward and convenient platform, was successfully fabricated for the visual detection of Hg^{2+} with a wide detection range from 5 nM to 50 μM.

1. Introduction

Heavy metal pollution has become an increasingly serious environmental problem. The mercury ion (Hg^{2+}), as a typical heavy metal ion, can be enriched and transmitted in the food chain, causing serious damage to the environment and human health.[1,2] Owing to the affinity of Hg^{2+} with thiol groups, toxic Hg^{2+} can cause dysfunctions, like destruction of the central nervous system and the endocrine system.[3–5] As recorded in the data,[6] the World Health Organization (WHO) has set the maximum contamination level of Hg^{2+} in drinking water as 6 ppb and the U.S. Environmental Protection Agency (EPA) has set the limit of Hg^{2+} as 2 ppb. Until now, a series of analysis techniques for the determination of Hg^{2+} have been developed, such as inductively coupled plasma mass spectrometry,[7] atomic absorption spectroscopy,[8] atomic emission spectrometry,[9] and surface-enhanced Raman scattering.[10] Due to the requirements of bulky and expensive instruments and well-trained operators, it is difficult to apply them in on-site applications. Furthermore, it is necessary for researchers to

develop a convenient and sensitive method to detect Hg^{2+}. In recent years, fluorescence analysis methods based on AuNCs for Hg^{2+} have emerged on account of the rapid response and high sensitivity of AuNCs towards Hg^{2+}. Fluorescent gold nanoclusters (AuNCs) with a size smaller than 3 nm exhibit molecule-like properties and show discrete electronic states.[11,12] By taking advantage of the 5d^{10}–5d^{10} interaction between Hg^{2+} and Au$^+$, AuNCs with different protecting agents were developed as the fluorescent materials to detect Hg^{2+}.[13] For example, Shang *et al.* rapidly synthesized dihydrolipoic acid (DHLA) capped fluorescent gold nanoclusters (DHLA-AuNCs) by the microwave-assisted method for the detection of Hg^{2+}.[14] Yang and co-workers utilized folic-acid-capped gold nanoclusters (FA-AuNCs) for the detection of mercury (Hg^{2+}) and methylmercury (CH$_3$Hg$^+$).[12] Zhang's group employed inexpensive chicken egg white (EW) as a reducing/capping reagent to develop the chicken egg white-protected gold nanoclusters (EW@AuNCs) with ultra-sensitive detection of Hg^{2+}.[15]

Besides, metal–organic frameworks (MOFs), which coordinate metal ions with organic ligands, are a class of crystalline microporous materials. MOFs possess fascinating features like high surface areas, tunable pore sizes and controllable surface functionalities; thus, more and more researchers exploit countless applications of MOFs including gas storage and separation, selective catalysis, drug delivery, and sensing.[16–20] Until now, various types of MOFs have been widely applied to fabri-

Jiangsu Province Hi-Tech Key Laboratory for Bio-medical Research, School of Chemistry and Chemical Engineering, Southeast University, Nanjing 211189, China. E-mail: snding@seu.edu.cn

†Electronic supplementary information (ESI) available. See DOI: 10.1039/c8an02414f

cate different kinds of sensors for analysis and detection. Lin and co-workers encapsulated branched poly-(ethylenimine)-capped carbon quantum dots (BPEI-CQDs) into the zeolitic imidazolate framework materials (ZIF-8) for the detection of Cu^{2+}.[21] Bai's group synthesized cysteine-functionalized MIL-101(NH$_2$) for efficient enrichment of N-linked glyco-peptides in cell lysate.[22] Yi *et al.* employed a Cy5-labeled 8–17 DNAzyme strand and a Cy3-labeled substrate strand to form a duplex probe adsorbing on the ZIF-8 surface for ratiometric fluorescence imaging of miRNAs.[23] Optically functionalized MOFs are the most attention-deserving because the inorganic or organic components can generate fluorescence, and other dimensional fluorescence functionalities could be combined with them to form novel materials.[17] Inspired by these studies, combining MIL-68(In)-NH$_2$ with AuNCs, the dual-emission ratiometric fluorescent sensor was proposed. MOFs, as an internal standard, provided a superior surface area, porous structure and fluorescence properties. Simultaneously, the AuNCs, as the response signal fluorophore, presented the sensing selectivity and fluorescence features. MOFs, as a desirable carrier, can enhance the amount of AuNC loading and amplify the signal intensity of AuNCs.[16] To further enhance the sensitivity of the sensor for the detection of Hg^{2+}, cysteine (Cys) was introduced to improve the fluorescence intensity of the sensor. It was worth noting that Cys could decrease the surface defects of AuNCs and played an important role in the sensing process due to its thiol groups (–SH).[24] Therefore, the dual-emission ratiometric fluorescence sensing platform, constructed of AuNCs/MIL-68(In)-NH$_2$/Cys, may present high sensing sensitivity and selectivity to various analytes.

Ratiometric fluorescent sensors are very suitable for the construction of small special equipment, which is easy to prepare, cheap, convenient, and highly sensitive.[25] Currently, microfluidic paper analytical devices (μPADs), first introduced by the Whitesides group in 2007,[26] as an innovative low-cost platform, have found applications in multiplexed analyte detection. μPADs are remarkable since porous hydrophilic paper as the three-dimensional (3D) microfluidic substrate makes liquid flow by capillary forces without the need to pump.[27,28] Meanwhile, hydrophobic barriers could identify liquid flow routes by depositing a hydrophobic material.[29] To confine liquid flow pathways, various paper designing methods, which have different channels, have been reported, such as inkjet printing,[30] wax printing[31] and screen-printing.[32] Wax printing, as the most attractive technique, possesses simply patterned paper and is of relatively low cost. After the reagents are modified and flowed through the hydrophilic region and the liquid has dried, the μPAD can be used for qualitative and quantitative chemical analyses, like high-throughput ion screening.

In this work, AuNCs/MIL-68(In)-NH$_2$/Cys were first synthesized by conjugating GSH-AuNCs and MIL-68(In)-NH$_2$, with a double fluorescence emission peak, which was accompanied by fluorescent AuNCs incorporated into fluorescent MIL-68(In)-NH$_2$ resulting in light pink fluorescence emission. The produced nanosensors after modification by cysteine further enhanced
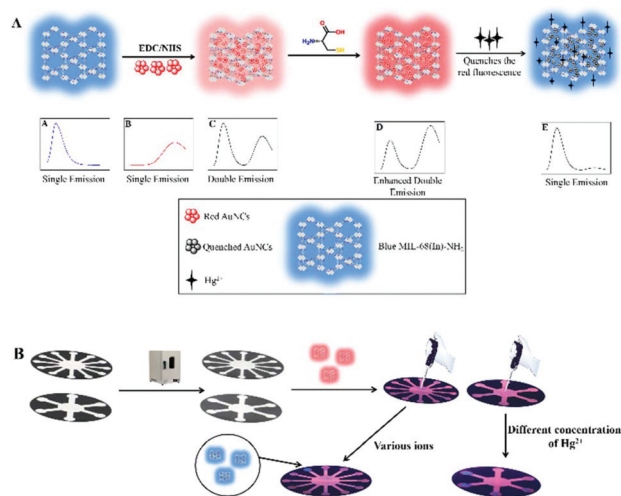
Scheme 1 (A) Schematic illustration of ratiometric fluorescent composites and the principles of the detection of Hg^{2+}. (B) The fabrication process of the μPAD for the detection of various ions and different concentrations of Hg^{2+}.

fluorescence emission at 668 nm of GSH-AuNCs and presented bright pink fluorescence. The sensor greatly reduced background signals and extremely improved sensitivity and selectivity. Meanwhile, the nanosensors had the advantages of Hg^{2+} detection (Scheme 1A). The ratiometric fluorescent sensor exhibited a lower LOD of 6.7 pM with a wide linear range of 20 pM–0.2 μM and 0.2 μM–60 μM for Hg^{2+} detection. Based on this, we developed a microfluidic paper-based analytical device (μPAD)[26] to achieve straightforward selection of different ions and detection of different concentrations of Hg^{2+} (Scheme 1B). Correspondingly, the μPAD was designed to be radially star-shaped with twelve detection reservoirs and six detection reservoirs. Furthermore, the time required for selective screening and Hg^{2+} detection did not exceed 10 s. The ratiometric fluorescent μPAD presented obvious color changes and had a wide Hg^{2+} concentration detection range from 5 nM to 50 μM. The observed good selectivity and sensitivity confirmed that the ratiometric fluorescent sensor can be further applied as a low-cost and attractive ion-screening μPAD to achieve further faster ion detection.

2. Experimental section

2.1 Chemicals and materials

Chloroauric acid (HAuCl$_4$·4H$_2$O), Cysteine (Cys), anhydrous methanol (CH$_3$OH, ≥99.5%), Nitric acid (HNO$_3$, ≥99.5%) and N,N-dimethylformamide (DMF, ≥99.5%) were purchased from Shanghai Sinopharm Chemical Reagent Co. Ltd (Shanghai, China). 2-Aminoterephthalic acid (H$_2$ATA, 99%) was received from Energy Chemical. N-Hydroxysuccinimide (NHS, 98%) was purchased from Sigma-Aldrich. 1-(3-Dimethylaminopropyl)-3-ethylcarbodiimide hydrochloride (EDC, 99%), Glutathione (GSH) and Indium nitrate hydrate (In(NO$_3$)$_3$·xH$_2$O, 99.99%)

were obtained from Aladdin. Phosphate buffer solutions (PBS, pH 5.0–11.0, 50 mM) were freshly prepared by varying the ratio of $NaH_2PO_4\cdot 2H_2O$ to $Na_2HPO_4\cdot 12H_2O$ before use. All chemicals and solvents were of analytical grade and were used without further purification. Double distilled water was used throughout.

2.2 Instrumentation and characterization

UV-vis absorption spectroscopy was performed on a UV-2600 spectrophotometer (Shimadzu Co.). The Fluoromax-4 fluorescence spectrofluorometer (Horiba, USA) was applied for fluorescence (FL) measurements. Transmission electron microscopy (TEM) measurements were conducted on a JEM-2100 transmission electron microscope (JEOL Ltd). Scanning electron microscopy (SEM) images were obtained using a FEI Sirion 200 scanning electron microscope. Zeta potential measurements were performed with a Marlvern Zetasizer (Nano ZS). The FT-IR spectrum was recorded using a Nicolet 5700 (USA) IR spectrometer in the range of $400–4000\ cm^{-1}$. The designed µPADs were printed by using a wax printer (ColorQube 8580N, Xerox, CT) on the filter paper (210 mm × 297 mm).

2.3 Synthesis of GSH-Au NCs

According to our previous work, the glutathione-stabilized gold nanoclusters (GSH-AuNCs) were synthesized with a slight modification.[33] The mixture of GSH (15 mM, 5 mL), and $HAuCl_4\cdot 4H_2O$ (1%, 2.06 mL) was under stirring for 2 min. After the addition of NaOH (1 M, 1 mL), the solution was incubated at 37 °C for 24 h. After washing with anhydrous methanol, the products were dried under vacuum, redispersed in double distilled water and stored at 4 °C for later use.

2.4 Synthesis of MIL-68(In)-NH₂

The indium-based metal–organic framework (MIL-68(In)-NH$_2$) was prepared by a solvothermal method by a little modification of the previous report.[34] In brief, the mixture of $In(NO_3)_3\cdot xH_2O$ and H_2ATA (the molar ratio between $In(NO_3)_3\cdot xH_2O$ and H_2ATA was 3 : 1) was added into DMF (6.2 mL), and the reaction solution was maintained at 125 °C for 5 h. After cooling to room temperature and washing several times with anhydrous methanol to remove the guest molecules in the pores, the samples were dried under vacuum at 100 °C for 12 h.

2.5 Synthesis of Au NCs/MIL-68(In)-NH₂ hybrid and cysteine enhanced the fluorescence

For the synthesis of the dual-emission ratiometric fluorescent nanocomposites from GSH-AuI, NCs and MIL-68(In)-NH$_2$ (AuNCs/MIL-68(In)-NH$_2$), the red emissive AuNCs were subsequently conjugated to MIL-68(In)-NH$_2$. Firstly, EDC/NHS solution was added to activate the carboxylic groups on the GSH-AuNC surface. Then, the MIL-68(In)-NH$_2$ suspension was supplied (the quality ratio between GSH-AuNCs and MIL-68 (In)-NH$_2$ was 100 : 1). Next, the mixture was kept shaking for 8 h in the dark. The dual-emission ratiometric fluorescent composites from AuNCs/MIL-68(In)-NH$_2$ modified with Cys

(AuNCs/MIL-68(In)-NH$_2$/Cys) could be enhanced, which resulted from the thiol groups (–SH) of Cys that were bonded to the surface of AuNCs. Typically, the Cys solution (the quality ratio between AuNCs/MIL-68(In)-NH$_2$ and Cys was 1 : 0.8) was added into the above solution and incubated at 40 °C under static conditions without stirring for 40 min. After cooling down, the AuNCs/MIL-68(In)-NH$_2$/Cys hybrid was dialyzed for 24 h with a dialysis membrane (100 000 MWCO). The visual color changes could be observed under a UV lamp (excitation wavelength at 365 nm). Followed by dialysis with deionized water, the sample could be taken directly for the detection of Hg^{2+} and visual detection on the paper could be achieved.

2.6 Detection of Hg²⁺ ions

To obtain a high sensitivity for Hg^{2+} detection, the pH value range from 5 to 11 was optimized through monitoring the emission intensity of the produced AuNCs/MIL-68(In)-NH$_2$ and AuNCs/MIL-68(In)-NH$_2$/Cys. Because Hg^{2+} tends to hydrolyze strongly in water, the solution of Hg^{2+} was prepared by dissolving an appropriate amount of $Hg(NO_3)_2$ in 0.1 M HNO_3 for the experiments.[35] All the fluorescence detection procedures were conducted in phosphate buffer solution (PBS, 5 mM, pH = 7.4, the most suitable condition) at room temperature. Comprehensively, adding different concentrations of Hg^{2+} solution into a series of 200 µL of the above dispersion makes the concentration gradient of the Hg^{2+} range from 0 µM to 60 µM. The final volume of the sample was adjusted to 500 µL with double distilled water, and then the mixture was shaken gently for 30 s, and the fluorescence spectra of the system were measured at an excitation wavelength of 370 nm.

2.7 Selectivity and interference experiments

To examine the selectivity of AuNCs/MIL-68(In)-NH$_2$/Cys probes to Hg^{2+}, the fluorescence intensity ratios ($FL_{668\ nm}/FL_{438\ nm}$) of AuNCs/MIL-68(In)-NH$_2$/Cys exposed to other competitive metal ions, such as Cd^{2+}, Zn^{2+}, Cu^{2+}, Fe^{3+}, Co^{2+}, Pb^{2+}, Cr^{3+}, Fe^{3+}, Mg^{2+}, Sn^{2+}, and Ni^{2+}, were studied under the same conditions. A volume of 200 µL of the above AuNCs/MIL-68 (In)-NH$_2$/Cys solution was mixed with 50 µL PBS solution (50 mM), followed by addition of a series of competitive metal cations. After that, deionized water was added to adjust the final volume (500 µL); the final solution was incubated for 60 s. Among them, the concentrations of Hg^{2+} were 60 µM and the concentrations of other metal ions were 150 µM. Finally, the mixture was added to a spectrophotometer trace quartz cuvette ready for fluorescence spectra recording. The visual color changes were observed under a UV lamp (excitation wavelength at 365 nm).

2.8 Practical detection of Hg²⁺ ions in lake and tap water

To assess the capability of the probes, the local lake sample, obtained from the Jiulong Lake, and the tap water have been tested. All water samples had the suspension removed by using 0.22 µm filters before use. After pretreatment, Hg^{2+} in water samples was detected by spiking known amounts of Hg^{2+} at four different concentrations (0.05, 40, 1×10^3, 2×10^4

μM) using AuNCs/MIL-68(In)-NH₂/Cys as the ratiomeric fluorescent sensor.

2.9 Visual detection of Hg^{2+} on the μPAD

The microfluidic paper-based analytical device (μPAD) in a 38 mm × 38 mm circle was designed using Adobe Illustrator. A sample reservoir was located at the center and twelve detection reservoirs were arranged regularly to detect various ions. A sample reservoir located at the center but with six star-shaped detection reservoirs was used to detect different concentrations of Hg^{2+}. Details of the design of the μPAD are presented in the ESI (Fig. S12†). As reported by Carrilho and co-workers,[31] the designed μPADs were printed on a sheet of filter paper (210 mm × 297 mm) by using a wax printer, and then dried at 150 °C for 50 s in an oven. The drying process caused the wax to pass through the paper, forming a 3D hydrophobic barrier to control the flow of liquid. As shown in Scheme 1B, each well-designed μPAD was cut down, and appropriate volumes of the AuNCs/MIL-68(In)-NH₂/Cys were added on the center reservoir until liquid diffused into each detection reservoir. After drying in an oven, the μPAD with 12-branch detection reservoirs was used for selectivity experiments. Namely, 5 μL of different metal ions was dropped on the twelve detection reservoirs. Meanwhile, the μPAD with 6-branch detection reservoirs was used for testing Hg^{2+} with various concentrations (0, 0.005, 0.05, 0.5, 5 and 50 μM), and the volume was also 5 μL. The visual fluorescence color can be easily observed under a 365 nm UV lamp. The fluorescence photos were taken by using a smartphone (iphone 6s plus). In the process of the experiment, a sheet of filter paper (210 mm × 297 mm) can produce 12 devices simultaneously at a cost of $ 0.0397 each.

3. Results and discussion

3.1 Characterization of GSH-Au NCs, MIL-68(In)-NH₂

The prepared red-emitting GSH-AuNCs were characterized by transmission electron microscopy (TEM), which showed clearly both the size and surface morphology. The TEM image in Fig. S1A† revealed that GSH-AuNCs had tiny spherical structures with decent dispersion. Meanwhile, it was clearly observed from HRTEM that the lattice spacing of GSH-AuNCs was 0.231 nm. As shown in Fig. S1B,† the mean diameter was calculated to be 1.6 nm. Such a result was highly consistent with the previous report that the sizes of GSH-AuNCs were observed to be smaller than 2 nm.[36–38] Fig. S2† displays a broad absorption before 400 nm but no absorbance peak around 500 nm existed, which demonstrated that highly purified AuNCs have been obtained without big particles or bulk metals as by-products.[33] Meanwhile, the product showed a red, broad emission peak centered at 678 nm (Fig. S3†).

The blue-emitting MIL-68(In)-NH₂ was characterized by scanning electron microscopy (SEM). The image showed that the composites showed a well-dispersed and willow leaf-like structure, which may be attributed to the formation of building blocks of the MIL-68(In)-NH₂ crystals during the synthesis

(Fig. S4†).[39] The FTIR spectra (Fig. S5†) can confirm successful formation of MIL-68(In)-NH₂. The bands at 3490 and 3367 cm⁻¹ were assigned to the symmetric and asymmetric stretching of primary amines. Furthermore, the peak at 1256 cm⁻¹ was attributed to the stretching vibration of N–C.[40] Fig. S6† depicts that MIL-68(In)-NH₂ had a blue fluorescence emission peak centered at 428 nm.

3.2 Characterization of AuNCs/MIL-68(In)-NH₂/Cys

The TEM image proved the successful preparation of AuNCs/MIL-68(In)-NH₂. Fig. 1A shows the morphology of AuNCs/MIL-68(In)-NH₂, which indicated that MIL-68(In)-NH₂ maintained a willow leaf-like structure after the incorporation of AuNCs into the MOF framework and the AuNCs were highly dispersed on the MIL-68(In)-NH₂ substrate. The successful fabrication of composite materials was certified through zeta potential (Fig. S7†). MIL-68(In)-NH₂ synthesized from 2-aminoterephthalic acid retained significant amino groups out of the framework, which induced positive charges at the surface of MIL-68(In)-NH₂, and showed a positive charge of 14.1 ± 0.5 mV. Moreover, GSH-AuNCs showed a negative charge of −24.1 ± 1.2 mV. Combining with them, the zeta potential changed to −8.41 ± 2.6 mV. The zeta potential demonstrated that besides the role of covalent binding there might be possible electrostatic binding between GSH-AuNCs and MIL-68(In)-NH₂. Moreover, the fluorescence intensity of AuNCs was gradually enhanced with the concentration of MIL-68(In)-NH₂ slowly increased (Fig. S8†). Thus, the optimal ratio of AuNCs versus MIL-68(In)-NH₂ was 100 : 1. As illustrated in Fig. 1B, the strong fluorescence emission peak of MIL-68(In)-NH₂ centered at 428 nm (curve a), and the weak fluorescence emission peak of GSH-AuNCs centered at 678 nm (curve b). Predictably, AuNCs/MIL-68(In)-NH₂ showed two obvious fluorescence peaks, the
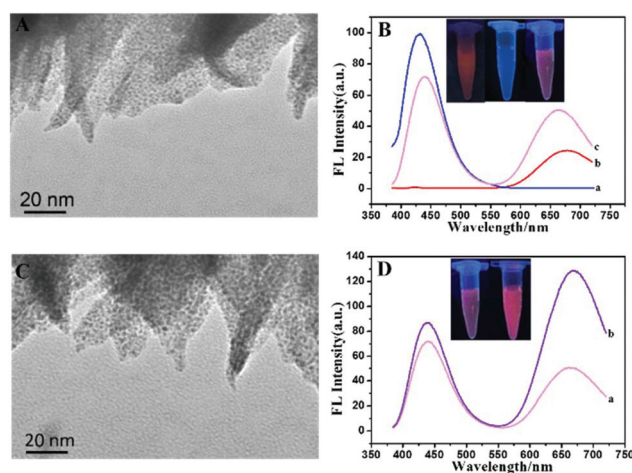

Fig. 1 (A) TEM image and (B) fluorescence emission spectra of AuNCs/MIL-68(In)-NH₂. Inset: Photographs of AuNCs, MIL-68(In)-NH₂ and AuNCs/MIL-68(In)-NH₂ under UV light (365 nm). (C) TEM image and (D) fluorescence emission spectra of AuNCs/MIL-68(In)-NH₂/Cys. Inset: Photographs of Au NCs/MIL-68(In)-NH₂ and AuNCs/MIL-68(In)-NH₂/Cys under UV light (365 nm).

emission intensity of MIL-68(In)-NH$_2$ decreased accompanied by the red shift to 438 nm, whereas the emission intensity of GSH-AuNCs increased double significantly with the blue shift to 663 nm (curve c). The porous structure and the large specific surface area of the MIL-68(In)-NH$_2$, result in the fluorescence enhancement of AuNCs. Besides, the inset images of Fig. 1B showed the red AuNCs, the blue MIL-68(In)-NH$_2$ and the light pink AuNCs/MIL-68(In)-NH$_2$ under UV (365 nm) illumination (from left to right corresponding to the three products). After cysteine (Cys) functionalization, as demonstrated in Fig. 1C, the TEM images of AuNCs/MIL-68(In)-NH$_2$/Cys verified that the framework showed no obvious change, while the size of AuNCs was clearly enlarged with good dispersion. It also proved the successful integration of AuNCs and cysteine. Fig. 1D shows that the peak of GSH-AuNCs at 668 nm was enhanced 2.6 times remarkably followed by the red shift 5 nm under the same excitation of 370 nm, while the emission intensity of MIL-68(In)-NH$_2$ at 438 nm remained stable and slightly enhanced. The formed AuNCs/MIL-68(In)-NH$_2$/Cys exhibited bright pink fluorescence (inset of Fig. 1D). Because of –SH of Cys bonded with the Au$^+$ in the AuNCs, Cys adsorbed on the surface of AuNCs, resulting in a further dramatic increase of the fluorescence intensity, while Cys can be tied to the amino-group on MIL-68(In)-NH$_2$ by its carboxyl group terminal, which induced slight strengthening of fluorescence emission at 438 nm via the restriction of intramolecular rotation (RIR) mechanism.[41] The two emission peaks were well separated by a wavelength distance of 230 nm, enhancing possibilities and sensitivity for ratiometric fluorescence detection.

By monitoring the fluorescence emission intensity of the produced AuNCs/MIL-68(In)-NH$_2$/Cys, the reaction time, temperature and the ratio of reactants were optimized, respectively. The results showed that incubation for 40 min at 40 °C of AuNCs/MIL-68(In)-NH$_2$ with cysteine served as the optimal conditions for the synthesis of AuNCs/MIL-68(In)-NH$_2$/Cys (Fig. S9†). The fluorescence intensity gradually stabilized with the increase of incubation time. However, after 40 °C, the fluorescence intensity decreased with the increase of temperature. The phenomenon can be attributed to higher temperature which was harmful to the reaction between cysteine and AuNCs, while the GSH on the surface of AuNCs would denature and aggregate when the reaction temperature exceeded 70 °C.[24] It could be also found that the ratio at 1 : 0.8 of AuNCs/MIL-68(In)-NH$_2$ to cysteine served as the optimal condition for the synthesis of AuNCs/MIL-68(In)-NH$_2$/Cys (Fig. S10†).

3.3 Detection of Hg^{2+} using the AuNCs/MIL-68(In)-NH$_2$/Cys

In the absence of Hg^{2+}, the AuNCs/MIL-68(In)-NH$_2$/Cys emitted double well-resolved fluorescence emission (peak at 438 nm and 668 nm) under a single wavelength excitation in optimized phosphate buffer solution (PBS, 5 mM, pH = 7.4) (Fig. S11†). Next, the dose–response of AuNCs/MIL-68(In)-NH$_2$/Cys to Hg^{2+} has been analyzed, when a certain concentration of Hg^{2+} was added, the red fluorescence was quenched and blue fluorescence of MIL-68(In)-NH$_2$ was only presented.

Regarding the fluorescence quenching mechanism, it was mainly caused by the heavy metal ion effect between Hg^{2+} (4f^{14}5d^{10}) and Au$^+$ (4f^{14}5d^{10}).[42–45] Moreover, owing to Cys that reacted with thiophilic Hg^{2+} and generated stable HS-Hg^{2+},[46] the fluorescence intensity at 668 nm of the sensors could also be reduced. Fig. 2A shows that in the presence of Hg^{2+} at the concentration ranging from 0 to 60 μM, the red fluorescence peak at 668 nm was continuously quenched, while the blue fluorescence peak at 438 nm was kept almost steady. When the concentration of Hg^{2+} was close to 60 μM, the emission intensity at 668 nm was quenched completely. Meanwhile, the fluorescence emission intensity at 438 nm was changed very slightly, which might be affected by thiophilic Hg^{2+} reaction with cysteine. As depicted in Fig. 2B, the fluorescence intensity ratios FL$_{668\ nm}$/FL$_{438\ nm}$ displayed a curve relationship versus the concentration of Hg^{2+} in the range of 0–60 μM, where FL$_{668\ nm}$ and FL$_{438\ nm}$ represented the FL intensities at 668 nm and 438 nm, respectively. The calibration curve was constructed under optimum conditions. Fig. 2C shows a good linearity response ranging from 20 pM to 200 nM with a correlation coefficient (R^2) of 0.993. The equation of linear regression could be expressed as: $Y = 1.577 − 2.269X$. Fig. 2D also presents a good linearity curve between 200 nM and 60 μM with R^2 at 0.998. The equation presented as: $Y = 1.125 − 0.014X$. In the above equations, X stands for the concentration of Hg^{2+} and Y stands for FL$_{668\ nm}$/FL$_{438\ nm}$. The limit of detection (LOD) was estimated to be 6.7 pM, at a signal-to-noise ratio (S/N) of 3, which is much lower than that of the maximum contamination level of Hg^{2+} in drinking water per-

Fig. 2 (A) Fluorescence emission spectra of AuNCs/MIL-68(In)-NH$_2$/Cys in the presence of Hg^{2+} with different concentrations (0, 2 × 10^{-4}, 5 × 10^{-3}, 0.02, 0.03, 0.04, 0.08, 0.12, 0.16, 0.2,2, 4, 6, 8, 10, 15, 20, 25, 30, 40, 50 and 60 μM). (B) Plot of the fluorescence intensity ratio (FL$_{668\ nm}$/FL$_{438\ nm}$) versus the concentration of Hg^{2+}. (C) The linear relationship between FL$_{668\ nm}$/FL$_{438\ nm}$ and the concentration of Hg^{2+} ranging from 20 pM to 0.2 μM. (D) The linear relationship between FL$_{668\ nm}$/FL$_{438\ nm}$ and the concentration of Hg^{2+} ranging from 0.2 μM to 60 μM. The error bars represent the standard deviation of three measurements (λ_{ex} = 370 nm, slit: 5/5 nm).

Table 1 Comparisons of the linear range and detection limit for Hg^{2+} with other materials

Materials	Linear ranges (nM)	Detection limit (LOD) (nM)	Ref.
EW@AuNCs	0.0446–5.9	0.02	15
BSA-AuNCs	1–20	9.8×10^{-3}	47
Metal ion-TSDRs	0.1–100	0.065	48
Lysozyme-AuNCs	$10–5 \times 10^3$	10	49
Mn-CDs	$100–5 \times 10^4$	1.6	50
BCDs and TGA-CdTe	$10–1.4 \times 10^3$	4.6	51
Thymine-CDs	$0–1.0 \times 10^6$	3.5×10^{-8}	52
AuNCs/ MIL-68(In)-NH$_2$/Cys	0.02–200, $200–6 \times 10^4$	1.7×10^{-3}	Our method

Table 2 Results of the detection of Hg^{2+} in Hg^{2+}-spiked real water samples using the ratiometric fluorescent probe AuNCs/MIL-68(In)-NH$_2$/Cys

Sample	Hg^{2+} spiked (nM)	Hg^{2+} found (nM)	Recovery (%)	RSD (%)
Lake	0.05	0.0546	109.2	2.6
	40	0.039×10^3	97.5	2.3
	1×10^3	1.102×10^3	110.2	3.4
Tap	2×10^4	1.994×10^4	99.7	1.5
	0.05	0.0482	96.4	2.8
	40	0.043×10^3	107.5	3.7
	1×10^3	0.913×10^3	91.3	2.5
	2×10^4	1.927×10^4	96.4	1.9

mitted by the World Health Organization (WHO, 6 ppb) and the U.S. Environmental Protection Agency (EPA, 2 ppb).[6] The methods of detection of Hg^{2+} by other fluorescent probes are shown in Table 1. The resulting dual-emission ratiometric fluorescent composites provided a wide linear range and a low LOD for the detection of Hg^{2+}, which were much better than those previously reported,[15,47–52] especially, the detection of Hg^{2+} adopted various AuNCs.

3.4 Selectivity of Au NCs/MIL-68(In)-NH$_2$/Cys for detecting metal ions

When applied in real analysis, the selectivity of AuNCs/MIL-68(In)-NH$_2$/Cys to the target metal ions over other pertinent metal ions (including Cd^{2+}, Zn^{2+}, Cu^{2+}, Fe^{3+}, Co^{2+}, Pb^{2+}, Cr^{3+}, Fe^{3+}, Mg^{2+}, Sn^{2+}, and Ni^{2+}) was essential.[53] In the experiment, other metal ions were 150 μM and Hg^{2+} was 60 μM under maximum concentration. The respective nitrate or chloride salts were prepared for stock solutions of other metal ions. The results of Fig. 3A depicted that only Hg^{2+} can induce a drastic decrease ($FL_{668 \, nm}/FL_{438 \, nm}$) of AuNCs/MIL-68(In)-NH$_2$/Cys. In contrast, other ions led to little fluorescence intensity change, even the concentration of other ions was higher than that of Hg^{2+}. Photographs of the aqueous solutions of the AuNCs/MIL-68(In)-NH$_2$/Cys after the addition of various ions under irradiation by UV light at 365 nm are given in Fig. 3B. Obviously, only Hg^{2+} could quench the red fluorescence and show the blue fluorescence. The experimental results showed

that the proposed probe in this paper has high selectivity for distinguishing Hg^{2+}.

3.5 Application in real samples

To assess the practicality of the proposed method to real samples, standard addition and recovery experiments were performed *via* the proposed sensing probe. Hg^{2+} standard solutions at known concentrations were spiked into the lake and tap samples, respectively. As listed in Table 2, the recoveries of all samples are in the range of 91.3–110.2% with a satisfactory consequence. In addition, the RSD definitely also indicated that the high accuracy and reliability could be achieved by the present sensing method. The fluorescent sensor based on AuNCs/MIL-68(In)-NH$_2$/Cys confirmed that the proposed method could achieve practical applications to detect Hg^{2+} in real samples.

3.6 Visual detection of Hg^{2+} on the μPAD

To further achieve rapidity and simplicity for detection, the new detection platform, microfluidic paper-based analytical device (μPAD), was selected to visually detect ions (Fig. S12†). The μPAD with twelve detection reservoirs (Fig. S13A†) was used for detecting various ions. Fig. S13B† shows that the μPAD presented light yellow after AuNCs/MIL-68(In)-NH$_2$/Cys was added and dried. Apparently, the μPAD with six detection reservoirs (Fig. S13C†), which was used for detecting Hg^{2+} at different concentrations, possessed the same light yellow color after treatment (Fig. S13D†). Under a 365 nm UV lamp, Fig. 4A and B present the selectivity of AuNCs/MIL-68(In)-NH$_2$/Cys on the μPAD to the target metal ions over other pertinent metal ions under the same conditions. Obviously, only treated with Hg^{2+}, the detection reservoir showed red fluorescence quenching and retained blue fluorescence. Fig. 4C and D indicate that the fluorescence conversion of AuNCs/MIL-68(In)-NH$_2$/Cys towards different concentrations of Hg^{2+}. With the increasing concentration of Hg^{2+} (0, 0.005, 0.05, 0.5, 5 and 50 μM), the red fluorescence appeared regularly quenching and there was increasingly strong blue fluorescence. All of these results confirmed that the μPAD provided a convenient and straightforward fluorescence platform for Hg^{2+} detection with high selectivity and sensitivity.
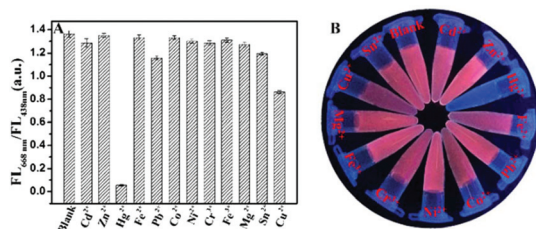

Fig. 3 (A) Fluorescence intensity ratios ($FL_{668 \, nm}/FL_{438 \, nm}$) of AuNCs/MIL-68(In)-NH$_2$/Cys to various metal ions. The bars represent the addition of different ions. The concentrations of different metal ions were 150 μM, except Hg^{2+} at 60 μM. (B) The image shows the corresponding fluorescence colors under a UV lamp (365 nm).

Fig. 4 Photographs of the μPAD (A) with the AuNCs/MIL-68(In)-NH₂/Cys, (B) and with the AuNCs/MIL-68(In)-NH₂/Cys responding to various metal ions under 365 nm UV light. The types of the ions are Fe²⁺, Cu²⁺, Pb²⁺, Co²⁺, Ni²⁺, Cr³⁺, Fe³⁺, Mg²⁺, Sn²⁺, Cd²⁺, Zn²⁺, and Hg²⁺ along the clockwise direction. Photographs of the μPAD (C) with the AuNCs/MIL-68(In)-NH₂/Cys under 365 nm UV light, (D) and with AuNCs/MIL-68(In)-NH₂/Cys responding to Hg²⁺ under 365 nm UV light. The concentrations of the Hg²⁺ solutions are 0, 0.005, 0.05, 0.5, 5 and 50 μM along the clockwise direction.

4.   Conclusion

In summary, the ratiometric fluorescent nanosensors were successfully developed, and AuNCs/MIL-68(In)-NH₂/Cys was constructed by AuNCs incorporated into MIL-68(In)-NH₂, and then further modified with Cys. Because MIL-68(In)-NH₂ has high porosity and specific surface area and Cys could reduce surface defects of AuNCs, the as-prepared AuNCs/MIL-68(In)-NH₂/Cys displayed bright pink fluorescence with double fluorescence emission peaks at 438 nm and 668 nm, and well-dispersed AuNCs. The fluorescence emission at 668 nm was enhanced 5.2 times remarkably compared to GSH-AuNCs. It was found that the enhanced pink fluorescence of AuNCs/MIL-68(In)-NH₂/Cys could be quenched by Hg²⁺ and two wide linear ranges from 20 pM to 0.2 μM and 0.2 μM to 60 μM with a lower detection limit of 8.7 nM were obtained. The sensor was successfully applied to recognize Hg²⁺ in real water samples with high levels of recoveries (91.3–110.2%). Additionally, the microfluidic paper-based analytical device (μPAD) was successfully fabricated to rapidly screen different ions with excellent selectivity and has been successfully applied to detect different concentrations of Hg²⁺ with the detection range from 5 nM–50 μM. Furthermore, we believe that the developed dual-emission fluorescent sensor and ratiometric fluorescent μPAD, with its satisfactory simplicity and sensitivity, would be propitious for applications in practical environmental analysis and biosensors.

Conflicts of interest

There are no conflicts to declare.

Acknowledgements

Notes and references

1 Y.-X. Qi, M. Zhang, A. Zhu and G. Shi, *Analyst*, 2015, **140**, 5656–5661.
2 Y.-C. Lu, J. Chen, A.-J. Wang, N. Bao, J.-J. Feng, W. Wang and L. Shao, *J. Mater. Chem. C*, 2015, **3**, 73–78.
3 G. Sener, L. Uzun and A. Denizli, *Anal. Chem.*, 2014, **86**, 514–520.
4 D. T. Quang and J. S. Kim, *Chem. Rev.*, 2010, **110**, 6280–6301.
5 D. W. Boening, *Chemosphere*, 2000, **40**, 1335–1351.
6 Z.-X. Wang and S.-N. Ding, *Anal. Chem.*, 2014, **86**, 7436–7445.
7 J. Allibone, E. Fatemian and P. J. Walker, *J. Anal. At. Spectrom.*, 1999, **14**, 235–239.
8 H. Erxleben and J. Ruzicka, *Anal. Chem.*, 2005, **77**, 5124–5128.
9 Y. Yu, Z. Du, M. Chen and J. Wang, *Angew. Chem.*, 2008, **120**, 8027–8030.
10 Y. Ding, S. Wang, J. Li and L. Chen, *TrAC, Trends Anal. Chem.*, 2016, **82**, 175–190.
11 E. Saouter and B. Blattmann, *Anal. Chem.*, 1994, **66**, 2031–2037.
12 J.-Y. Yang, T. Yang, X.-Y. Wang, M.-L. Chen, Y.-L. Yu and J.-H. Wang, *Anal. Chem.*, 2018, **90**, 6945–6951.
13 L.-Y. Chen, C.-W. Wang, Z. Yuan and H.-T. Chang, *Anal. Chem.*, 2015, **87**, 216–229.
14 L. Shang, L. Yang, F. Stockmar, R. Popescu, V. Trouillet, M. Bruns, D. Gerthsen and G. U. Nienhaus, *Nanoscale*, 2012, **4**, 4155–4160.
15 Y. Zhang, J. Jiang, M. Li, P. Gao, L. Shi, G. Zhang, C. Dong and S. Shuang, *Sens. Actuators, B*, 2017, **238**, 683–692.
16 X. Yang, Y.-Q. Yu, L.-Z. Peng, Y.-M. Lei, Y.-Q. Chai, R. Yuan and Y. Zhuo, *Anal. Chem.*, 2018, **90**, 3995–4002.
17 Y. Cui, Y. Yue, G. Qian and B. Chen, *Chem. Rev.*, 2012, **112**, 1126–1162.
18 N. L. Rosi, J. Eckert, M. Eddaoudi, D. T. Vodak, J. Kim, M. Keeffe and O. M. Yaghi, *Science*, 2003, **300**, 1127.
19 M. D. Allendorf, C. A. Bauer, R. K. Bhakta and R. J. T. Houk, *Chem. Soc. Rev.*, 2009, **38**, 1330–1352.
20 F. Cao, E. Ju, C. Liu, W. Li, Y. Zhang, K. Dong, Z. Liu, J. Ren and X. Qu, *Nanoscale*, 2017, **9**, 4128–4134.
21 X. Lin, G. Gao, L. Zheng, Y. Chi and G. Chen, *Anal. Chem.*, 2014, **86**, 1223–1228.
22 W. Ma, L. Xu, X. Li, S. Shen, M. Wu, Y. Bai and H. Liu, *ACS Appl. Mater. Interfaces*, 2017, **9**, 19562–19568.
23 J.-T. Yi, T.-T. Chen, J. Huo and X. Chu, *Anal. Chem.*, 2017, **89**, 12351–12359.

24 M.-L. Cui, J.-M. Liu, X.-X. Wang, L.-P. Lin, L. Jiao, L.-H. Zhang, Z.-Y. Zheng and S.-Q. Lin, *Analyst*, 2012, **137**, 5346–5351.

25 J. F. da Silveira Petruci and A. A. Cardoso, *Anal. Chem.*, 2016, **88**, 11714–11719.

26 A. W. Martinez, S. T. Phillips, M. J. Butte and G. M. Whitesides, *Angew. Chem., Int. Ed.*, 2007, **46**, 1318–1320.

27 H. Liu and R. M. Crooks, *J. Am. Chem. Soc.*, 2011, **133**, 17564–17566.

28 T. Akyazi, A. Tudor, D. Diamond, L. Basabe-Desmonts, L. Florea and F. Benito-Lopez, *Sens. Actuators, B*, 2018, **261**, 372–378.

29 Y. S. Kim, Y. Yang and C. S. Henry, *Sens. Actuators, B*, 2018, **255**, 3654–3661.

30 K. Abe, K. Suzuki and D. Citterio, *Anal. Chem.*, 2008, **80**, 6928–6934.

31 E. Carrilho, A. W. Martinez and G. M. Whitesides, *Anal. Chem.*, 2009, **81**, 7091–7095.

32 S. Wang, L. Ge, X. Song, J. Yu, S. Ge, J. Huang and F. Zeng, *Biosens. Bioelectron.*, 2012, **31**, 212–218.

33 C.-L. Zheng, Z.-X. Ji, J. Zhang and S.-N. Ding, *Analyst*, 2014, **139**, 3476–3480.

34 L. Wu, M. Xue, S.-L. Qiu, G. Chaplais, A. Simon-Masseron and J. Patarin, *Microporous Mesoporous Mater.*, 2012, **157**, 75–81.

35 J. Yao, K. Zhang, H. Zhu, F. Ma, M. Sun, H. Yu, J. Sun and S. Wang, *Anal. Chem.*, 2013, **85**, 6461–6468.

36 Y. Yu, Z. Luo, D. M. Chevrier, D. T. Leong, P. Zhang, D.-E. Jiang and J. Xie, *J. Am. Chem. Soc.*, 2014, **136**, 1246–1249.

37 Z. Luo, V. Nachammai, B. Zhang, N. Yan, D. T. Leong, D.-E. Jiang and J. Xie, *J. Am. Chem. Soc.*, 2014, **136**, 10577–10580.

38 R. Jin, *Nanoscale*, 2010, **2**, 343–362.

39 Y. Pi, X. Li, Q. Xia, J. Wu, Z. Li, Y. Li and J. Xiao, *Nano Res.*, 2017, **10**, 3543–3556.

40 R. Liang, L. Shen, F. Jing, W. Wu, N. Qin, R. Lin and L. Wu, *Appl. Catal., B*, 2015, **162**, 245–251.

41 T. Du, H. Zhang, J. Ruan, H. Jiang, H.-Y. Chen and X. Wang, *ACS Appl. Mater. Interfaces*, 2018, **10**, 12417–12423.

42 P. Pyykkö, *Angew. Chem., Int. Ed.*, 2004, **43**, 4412–4456.

43 J. Xie, Y. Zheng and J. Y. Ying, *Chem. Commun.*, 2010, **46**, 961–963.

44 X. Xu, Y.-F. Li, J. Zhao, Y. Li, J. Lin, B. Li, Y. Gao and C. Chen, *Analyst*, 2015, **140**, 7841–7853.

45 J.-J. Feng, H. Huang, D.-L. Zhou, L.-Y. Cai, Q.-Q. Tu and A.-J. Wang, *J. Mater. Chem. C*, 2013, **1**, 4720–4725.

46 K. Severin, R. Bergs and W. Beck, *Angew. Chem., Int. Ed.*, 1998, **37**, 1634–1654.

47 I. Onyido, A. R. Norris and E. Buncel, *Chem. Rev.*, 2004, **104**, 5911–5930.

48 S. Wang, X. Li, J. Xie, B. Jiang, R. Yuan and Y. Xiang, *Sens. Actuators, B*, 2018, **259**, 730–735.

49 H. Wei, Z. Wang, L. Yang, S. Tian, C. Hou and Y. Lu, *Analyst*, 2010, **135**, 1406–1410.

50 Q. Xu, R. Su, Y. Chen, S. Theruvakkattil Sreenivasan, N. Li, X. Zheng, J. Zhu, H. Pan, W. Li, C. Xu, Z. Xia and L. Dai, *ACS Appl. Nano Mater.*, 2018, **1**, 1886–1893.

51 F. Ghasemi, M. R. Hormozi-Nezhad and M. Mahmoudi, *Sens. Actuators, B*, 2018, **259**, 894–899.

52 Y. Li, Z.-Y. Zhang, H.-F. Yang, G. Shao and F. Gan, *RSC Adv.*, 2018, **8**, 3982–3988.

53 C. Zou, M. F. Foda, X. Tan, K. Shao, L. Wu, Z. Lu, H. S. Bahlol and H. Han, *Anal. Chem.*, 2016, **88**, 7395–7403.